



Cite this: *RSC Adv.*, 2023, **13**, 14782

## Photoluminescence, antibacterial, X-ray/gamma ray absorption, supercapacitor and sensor applications of $\text{ZrTiO}_4$ nanorods

Akshay S,<sup>ab</sup> Y. S. Vidya,<sup>id</sup> \*c H. C. Manjunatha,<sup>id</sup> \*d S. C. Prashantha,<sup>\*b</sup> Nagaraju Kottam,<sup>e</sup> K. N. Sridhar,<sup>f</sup> P. S. Damodara Gupta<sup>d</sup> and C. Mahendrakumar<sup>g</sup>

In the present communication,  $\text{ZrTiO}_4$  nanoparticles (NPs) are synthesized by the solution combustion method using urea (ZTOU) and oxalyl dihydrazide (ZTODH) as fuel and calcined at 700 °C. The synthesized samples were characterized with different techniques. Powder X-ray diffraction studies show the presence of diffraction peaks corresponding to  $\text{ZrTiO}_4$ . In addition to these peaks, a few additional peaks corresponding to the monoclinic and cubic phases of  $\text{ZrO}_2$  and the rutile phase of  $\text{TiO}_2$  are observed. The surface morphology of ZTOU and ZTODH consists of nanorods with different lengths. The TEM and HRTEM images confirm the formation of nanorods along with NPs, and the estimated crystallite size matches well with that of PXRD. The direct energy band gap was calculated using Wood and Tauc's relation and was found to be 2.7 and 3.2 eV for ZTOU and ZTODH respectively. The photoluminescence emission peaks ( $\lambda = 350$  nm), CIE and CCT of ZTOU and ZTODH clearly confirm that the present nanophosphor might be a good nanophosphor material for blue or aqua green light emitting diodes. Furthermore, antibacterial activity and a viability test were conducted on two food borne pathogens. The X-ray/gamma ray absorption properties are also studied, which clearly show the  $\text{ZrTiO}_4$  might be a good absorbing material. Furthermore, cyclic voltammetry (CV) analysis of ZTOU nanorods shows very good redox peaks compared to that of ZTODH. From the electrochemical impedance spectroscopy (EIS) measurements, the charge-transfer resistances for prepared nanorods ZTOU and ZTODH are found to be 151.6 Ω, and 184.5 Ω respectively. The modified graphite electrode with ZTOU shows good sensing activity for both paracetamol and ascorbic acid, compared to ZTODH.

Received 10th February 2023  
 Accepted 13th April 2023

DOI: 10.1039/d3ra00908d  
[rsc.li/rsc-advances](http://rsc.li/rsc-advances)

### 1. Introduction

Advanced ceramic materials, which could be single crystals, entirely vitreous, or a combination of two or more crystalline phases<sup>1,2</sup> find diverse applications in modern technology. Among the different ceramic materials the most popular are titanates with the molecular formula  $\text{ABO}_3/\text{ABO}_4$  where A and B

are two different metallic cations. They have attracted attention due to their polyvalent properties for piezoelectric, ferroelectric, optoelectronic and photocatalytic applications. Among the titanates,  $\text{ZrTiO}_4$  (ZTO) a mixture of zirconia and titania, is a type of  $\text{ABO}_4$  compound that has gotten a lot of interest from scientists. Even though they exhibit a heterogeneous phase, the composite of these two oxides exhibits a single orthorhombic phase. Due to this single phase, ZTO shows excellent optical, electronic, hardness, refractive indices, durability, low absorption etc., properties.<sup>3</sup>

Structural order and disorder present in real materials are going to modify their electrical and optical characteristics, which can be useful in technological applications.<sup>2,4</sup> The conduction band of titanates is dominated by titanium 3d, while the valence band is dominated by oxygen 2p. The bands are separated by at least 3 eV, allowing these materials to absorb solely UV light, which may lead to new optoelectronic devices, notably those for use in the creation of green or blue light emission diodes (LEDs) or laser diodes. The optical absorption corresponds to a charge-transfer transition between  $\text{O}^{2-}$  and  $\text{Ti}^{4+}$ .<sup>5,6</sup> Many researchers have been examining titanates' electrical structures and photophysical properties and focusing on

<sup>a</sup>Department of Physics, Maharani Lakshmi Ammanni College for Women, Autonomous Malleshwaram, Bengaluru, 560012, Karnataka, India

<sup>b</sup>Department of Physics, East West Institute of Technology, Bengaluru, 560091, Karnataka, India. E-mail: [scphysics@gmail.com](mailto:scphysics@gmail.com)

<sup>c</sup>Department of Physics, Lal Bahadur Shastri Government First Grade College, RT Nagar, Bangalore, 560032, Karnataka, India. E-mail: [vidays.phy@gmail.com](mailto:vidays.phy@gmail.com)

<sup>d</sup>Department of Physics, Government College for Women, Kolar, 563101, Karnataka, India. E-mail: [manjunathhc@rediffmail.com](mailto:manjunathhc@rediffmail.com)

<sup>e</sup>Department of Chemistry, M S Ramaiah Institute of Technology affiliated to Visvesvaraya Technological University, Belgaum, Bengaluru, 560054, Karnataka, India

<sup>f</sup>Department of Physics, Government First Grade College, Kolar, 563101, Karnataka, India

<sup>g</sup>Department of Biotechnology, Government First Grade College, Kolar, 563101, Karnataka, India



studying their photoluminescence (PL) emissions. The PL emissions in titanates are considered to be closely related to the crystal structure, and they are responsible for the disorders in metal–oxygen polyhedra.<sup>4,7,8</sup> Lokesh *et al.*<sup>9</sup> studied the effect of copper doping on the structural and PL properties of zinc titanates. BaTiO<sub>3</sub> shows a PL band centred at 500 nm when it is excited with UV light.<sup>10</sup> Although, extensive work has been carried out on the PL properties of titanates, till now, only a few works are available with respect to the PL properties of ZrTiO<sub>4</sub>.<sup>11</sup>

Furthermore, titanates are inorganic ion exchangers that can alter the electronic states and band structure without changing the original morphology and bind various metal ions.<sup>12,13</sup> In the nano and medical science era, generating less expensive nanopowders with appropriate antibacterial capabilities would be of considerable importance. In general, metal NPs are the most promising antibacterial agents. But these metal ions were found to have many toxic effects on the environment as well as aggregate easily in the medium that alters their cytotoxicity.<sup>14</sup> To overcome these disadvantages, numerous studies have been conducted to improve the antibacterial agents activity. Due to its desirable features, such as corrosion resistance, improved mechanical qualities, and good biocompatibility, titanium (Ti) based alloys are standard biomaterials used extensively in the fields of orthopaedics and dentistry.<sup>15</sup> Few titanates are used as exchangers for the removal of radio nuclides from nuclear wastes<sup>16,17</sup> and few of them are studied for their capacity to deliver therapeutic ions to target cells or to inhibit bacterial growth.<sup>18,19</sup> The need for better mechanical properties of biomaterial implants, both in dental and orthopedic applications, has prompted researchers to investigate titanium alloys containing zirconium (TiZr), which have higher tensile and fatigue strengths than pure titanium.<sup>20–22</sup> Stoian *et al.*,<sup>20</sup> studied the interaction of nanomixtures of Zr and Ti and also the cell behavior of bacteria on TiZr alloy depending on their structure after anodizing at various potentials and annealing settings. Mohseni *et al.*,<sup>23</sup> synthesized barium zirconate titanate and tested it on *E. coli*, *K. pneumoniae*, *M. luteus* and *S. aureus* as representative Gram-negative and Gram-positive bacteria. From the literature, only a few studies have been reported on the antibacterial activity of ZTO.

Eventually, developing novel, sophisticated materials for nuclear science will become increasingly important due to the increased demand for improved shielding in severe situations.<sup>24</sup> Radiation shielding materials possess good mechanical properties, long term reliability, and suitable thermo-physical characteristics. Because of its high density and high atomic number, lead (Pb) has long been regarded as the ideal and traditional material for effective radiation shielding, particularly for blocking the penetration of gamma rays and X-rays.<sup>25</sup> However, one of the disadvantages of these Pb-based materials is their toxicity, as well as the possibility of leakage owing to damage, cracks, and the age of these matrices. As a result, other less hazardous and non-Pb elements with a high atomic number, such as bismuth (Bi), tungsten (W), barium (Ba), tin (Sn), cadmium (Cd), gadolinium (Gd), copper (Cu), and titanium (Ti), must be explored and introduced as Pb substitutes.<sup>26,27</sup> Thus, there is a need to develop low-toxicity and non-

Pb shielding materials to protect individuals from hazardous X-ray radiation. X-ray/gamma absorption properties are quantified by a set of parameters. Correct values of X-ray/gamma ray radiation interaction parameters are found to be extremely important in a variety of domains, including nuclear diagnosis, radiation protection, nuclear medicine, radiation dosimetry and radiation biology among others.<sup>24</sup> Saini *et al.*,<sup>28</sup> report the EMI shielding properties of high permittivity polyaniline–barium titanate nanocomposites. There is still much research going on to develop valuable materials to be used in radiation shielding by reporting their X-ray/gamma ray shielding parameters.<sup>29–32</sup> Herein, to address these research gaps and meet the demand for developing lightweight and Pb-free X-ray/gamma shielding materials, shielding parameters are discussed.

In addition to this, titanates find an important applications in electrochemical devices such as sensors. For chemical sensors, dynamic electrochemistry is a well-known and adaptable transduction technique.<sup>33,34</sup> Drug monitoring plays a vital role in drug quality control, and this has a significant impact on public health, so developing easy, sensitive, and accurate methods for detecting active components is critical.<sup>35</sup> Since the drug is electroactive, electrochemical approaches can be viewed as a strong alternative to existing methods.<sup>36–38</sup> Generally, carbon based materials are the most efficient supercapacitors titanates are the efficient charging materials, having a high surface area and pores appropriate to the size of ions, which are required for efficient charging of the electrical double layer, which is critical for supercapacitors. Carbon, conducting polymers and transition metal oxides are the most commonly used active electrode materials.<sup>39–41</sup> But, still structural flexibility and stability, quick cation diffusion under high charge–discharge rates and environmental friendliness are the areas where active materials are being improved. In this regard, research work has been carried out by many researchers using titanates as an alternative to the other materials.<sup>42,43</sup>

According to the experimental approach, the time required for synthesizing, the temperature at which the process is carried out, the presence of solvent, the presence of ultrasound, or the use of microwave radiation all affect the properties of the product.<sup>44</sup> Researchers have concentrated on developing new synthesis methods such as the hydrothermal method,<sup>45,46</sup> microwave assisted synthesis,<sup>47</sup> sol gel route<sup>48,49</sup> for producing titanate based NPs of varied sizes and morphologies. Among these conventional methods, the solution combustion process produces a significant amount of gaseous waste. Such gasification causes substantial expansion of the solid product and a rapid drop in temperature following the reaction, resulting in a porous and finely dispersed solid product. Thus, in the present study, a ZTO sample was synthesized by using the solution combustion method. The solution combustion method has been frequently used to produce simple and complicated oxides with desired morphologies.<sup>50</sup>

In the present communication, despite the fact that extensive research has been done on the material strengths of ZTO, the fundamental properties that define the use of ceramics as a nanophosphor material in display technology, an



antibacterial agent, X-ray/gamma ray absorber, and a sensor material (ascorbic acid and paracetamol), supercapacitor properties are still unknown. Moreover, the use of different types of fuels plays an important role in the solution combustion method. The fuel affects the size, morphology and purity as well as the optical and sensor properties.<sup>51</sup> In order to shed some light on the understanding of the optical, biocompatibility, sensor and supercapacitor properties – ZrTiO<sub>4</sub> NPs are synthesized by the solution combustion method using two different fuels such as urea and Oxalyl dihydrazide and calcined at 700 °C. The synthesized samples were characterized with different techniques such as powder X-ray diffraction (PXRD), scanning electron microscopy (SEM), transmission electron microscopy (TEM), Fourier transmission infrared spectroscopy (FTIR) and UV-visible spectroscopic analysis was carried out.

## 2. Materials and experimental section

### 2.1 Materials

All the used chemicals for synthesis of ZTO were of analytical grade and used without further purification. Titanium-tetra-butoxide (Ti(OCH<sub>2</sub>CH<sub>2</sub>CH<sub>2</sub>CH<sub>3</sub>)<sub>4</sub>), zirconyl nitrate ZrO(NO<sub>3</sub>)<sub>2</sub>, urea and oxalyl dihydrazide (ODH) of S.D Fine chemicals, Bombay, India. Initially, titanium-tetra-butoxide is converted to titanyl nitrate by mixing 5.4 ml of titanium-tetra-butoxide to 1 : 1 HNO<sub>3</sub> (nitric acid:water). The stoichiometric amount of zirconyl nitrate, titanyl nitrate and urea/ODH used for the combustion was calculated using total oxidizing and reducing valences of the compounds. All these heterogeneous mixture were taken in a cylindrical crucible. This mixture was placed in preheated muffle furnace maintained at a temperature of 500 ± 10 °C. The resulting solution was initially boiled, subsequently dehydrated with elimination of gases like carbon dioxide, nitrogen and water vapour followed by the formation of final product. The resulted product was calcined at 700 °C for 2 h and then it is cooled to the room temperature and collected. The flowchart for the synthesis of ZTO by using different fuels urea (ZTOU) and ODH (ZTODH) are shown in the Fig. 1.

The final products were characterized using Shimadzu Powder X-ray diffractometer (PXRD). The diffraction patterns were recorded at room temperature using Cu K $\alpha$  (1.541 Å) radiation with nickel filter in the 2 h range 20–70° at a scan rate of 2° min<sup>-1</sup>. The morphological features and particle size were studied by scanning electron microscopy (SEM, Hitachi-3000). FTIR studies of the NPs were performed with a PerkinElmer Frontier FTIR spectrometer. The UV-visible absorption

spectrum was recorded on PerkinElmer UV-visible Spectrophotometer. The PL measurements were performed on a Horiba Fluorolog Spectrofluorimeter at room temperature. The measurement of X-ray/gamma ray shielding properties and its theoretical evaluation was explained briefly in our previous work.<sup>52</sup>

### 2.2 Antimicrobial properties of ZTOU and ZTODH NPs

**2.2.1 Bacterial cultures.** Bacterial cultures namely *Bacillus cereus* and *Pseudomonas aeruginosa* were obtained from the Department of studies and research in biochemistry, Mangalore University. The above cultures were grown in nutrient agar media (HiMedia, Mumbai, India) at 37 °C. Each bacterial strain was transferred from stored slants at 4–5 °C to 10 ml nutrient broth and cultivated overnight at 37 °C for 24 h. Growth condition for the bacterial culture was kept under dark incubator. Pre-culture was prepared by transferring 1 ml of this culture to 9 ml nutrient broth and cultivated for 48 h. The bacterial cells were harvested by centrifugation (1200 g, 5 min), followed by washing with saline and finally it was suspended in 9.9 ml of sterilized saline.

**2.2.2 Growth inhibition assay.** Effect of ZTOU and ZTODH on the growth of different bacteria was studied by the method of Jayaprakasha *et al.*<sup>53</sup> Appropriate quantities of compounds were transferred into different flasks containing 20 ml of sterilized nutrient agar to obtain final concentrations of 0.5, 1.0, 2.0, 5.0, 10.0, 15.0 mg mL<sup>-1</sup>. A control sample was prepared by transferring an equivalent amount of 0.1 M citrate buffer of pH 5.2 to 20 ml of melted nutrient agar. 100 µL (about 104 cfu mL<sup>-1</sup>) of each bacterium was inoculated into flasks under aseptic conditions. The medium was then poured into sterilized Petri-plates in quadruplet and incubated at 37 °C for 24 h. The colonies developed after incubation were counted and expressed as colony forming units per ml of culture (cfu mL<sup>-1</sup>). The inhibitory effect was calculated using the following formula,

$$\text{Percentage of Inhibition} = \left(1 - \frac{T}{C}\right) \times 100 \quad (1)$$

where  $T$  = cfu mL<sup>-1</sup> of test sample and  $C$  = cfu mL<sup>-1</sup> of control. The minimum inhibitory concentration (MIC) was reported as the lowest concentration of the compound capable of inhibiting the complete growth of the bacterium tested.

**2.2.3 Zone of inhibition test.** This test was carried out for ZTOU and ZTODH NPs. The above bacterial cultures were inoculated on nutrient agar media by spread plate method.<sup>53</sup> Small circular wells were dug into agar plates using the back end of the 100 µL pipette tip. 50 mg of each ZTOU and ZTODH samples were suspended in 100 µL of 0.1 M citrate buffer and placed in the wells. The plates were then incubated at 37 °C for 24 hours. The diameter of the zone of inhibitor was then measured after the incubation.

### 2.3 X-ray/gamma absorption properties

The synthesized nano particles were studied for absorption properties of X-ray/gamma ray. We have measured and also

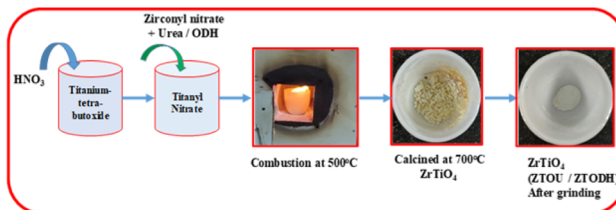


Fig. 1 Flow chart for the synthesis of ZTOU and ZTODH nanorods.



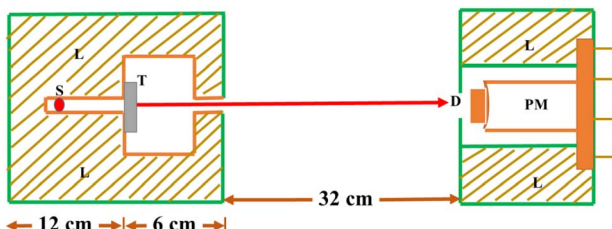


Fig. 2 Schematic diagram of the experimental setup (S: source position, T: target sample, L: lead shielding, D: detector, PM: photomultiplier).

theoretically evaluated. Gamma rays of energy 0.6615 MeV ( $^{137}\text{Cs}$ ), 1.173, 1.332 MeV ( $^{57}\text{Co}$ ), 0.511, 0.081 MeV ( $^{22}\text{Na}$ ), 0.276 and 0.356 MeV ( $^{133}\text{Ba}$ ) emitted by the radioactive sources, were collimated and detected by NaI (Tl) crystal detector mounted on a photo multiplier tube housed in a lead chamber and a sophisticated PC based MCA is used for the detection purpose. The schematic view of the experimental set up used for the measurement of X-ray/gamma ray absorption properties is given in Fig. 2. The sample was directly attached to the opening of the lead shield where source is placed. The integral intensities,  $I_0$  and  $I$  of the beam before and after passing through the sample are measured for sufficient time. Mass attenuation coefficient of the sample is then estimated using the relation:

$$\left(\frac{\mu}{\rho}\right)_c = \left(\frac{1}{t\rho}\right) \ln\left(\frac{I_0}{I}\right) \quad (2)$$

where  $t$  and  $\rho$  are the thickness and density of the sample respectively. When we record the spectrum without any target the spectral lines that we get is only due to the radioactive source, in the present case it is the gamma radiation. But when we keep the target due to interaction of gamma rays with that of the target material there will be an emission of secondary X-rays. We can distinguish this if record the two spectrum *viz.*, with sample between the source and the detector and another only with the source.

#### 2.4 Electrochemical studies

For electrochemical studies and sensor studies, the electrochemical analyser of CHI608E potentiostat having tri electrode pattern was chosen. Electrochemical impedance studies (EIS) were performed with 5 mV of AC amplitude with frequency range of 1 Hz to 1 MHz.

**2.4.1 Preparation of graphite paste electrode.** To make the graphite modified working electrode for the electrochemical work, a semi-paste was made by mixing a mixture of ZTOU/ZTODH (0.075 g), graphite powder (0.375 g) and silicon oil (3 drops for binding) in a mortar and pestle for 10 minutes. In a Teflon tube, this semi-paste mixture was filled snugly and entirely without any air gaps. The final surface area was smoothed using tissue paper to avoid the uneven surface area and minor gaps/holes.

**2.4.2 Sample preparation for sensor.** The paracetamol content in Dolo-650 tablet (commercially available) was measured using a graphite modified electrode. This tablet was

dissolved in 10 ml of double distilled water and the solution was made to the necessary concentration. The same procedure is followed for the ascorbic acid powder also. During the experiment, the produced solutions were mixed with the needed amount of electrolyte (from 1 to 7 mM).

### 3. Results and discussion

In the present study, ZTO samples are synthesized by economical solution combustion method using urea and ODH as a fuel. The obtained products are calcined at 700 °C. To know the phase purity, functional group, surface morphology, structural analysis and energy band gap, the synthesized sample were characterized by using PXRD, SEM, EDAX, FTIR and UV-visible spectrophotometer. Photoluminescence properties are discussed in detail for display applications. For the first time, the effect of two different fuels on other applications such as antibacterial, X-ray/gamma ray shielding properties, super capacitor and sensor applications are discussed in detail.

#### 3.1 PXRD analysis

PXRD is one of the most extensively used techniques for the characterization of NPs. It provides the information about the crystalline structure, phase nature, lattice parameters and crystalline grain size. Fig. 3a and b depicts the PXRD pattern of ZTOU and ZTODH respectively. The PXRD diffraction pattern shows the characteristic Bragg's reflection of orthorhombic phase of ZTOU and ZTODH and matches well with the JCPDS file number 74-1504 with  $a = 5.035 \text{ \AA}$ ,  $b = 5.487 \text{ \AA}$  and  $c = 4.801 \text{ \AA}$ . ZTOU shows pure phase of the sample whereas very few diffraction peaks corresponding to tetragonal phase of  $\text{ZrO}_2$  are observed. The PXRD pattern of ZTOU consists Bragg's reflections (011), (111), (020), (200), (112), (121), (022), (220), (202), (113), (222), (023) and (132) planes are observed at 24.73, 30.65, 33.50, 35.63, 41.54, 43.44, 44.15, 48.77, 50.31, 56.22, 59.30, 60.84

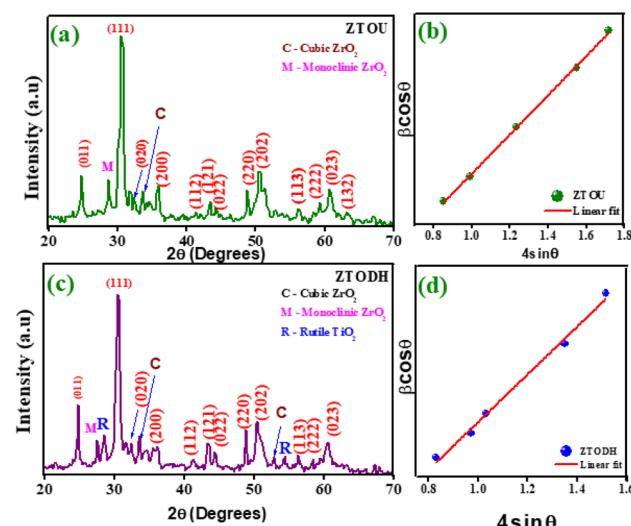


Fig. 3 (a) PXRD pattern of ZTOU, (b) W-H plot of ZTOU, (c) PXRD pattern of ZTODH and (d) W-H plot of ZTODH nanorods.

Table 1 Crystallite size and other structural parameters of ZTOU and ZTODH nanorods

Sample	Crystallite size (nm)		Strain $\times 10^{-3}$	Dislocation density (li nm $^{-2}$ )	Stacking fault
	Scherrer's	W-H plot			
ZTOU	6	8	3.262	2.77	3.31
ZTODH	8	10	4.2852	1.56	3.34

and  $63.10^\circ$   $2\theta$  values. In addition to all these peaks ( $-111$ ) and ( $200$ ) planes corresponding to monoclinic and cubic phase of  $\text{ZrO}_2$  are observed at  $27.08$  and  $34.06^\circ$  respectively. No traces of additional peaks corresponding to other impurities such as anatase, brukite and rutile phase of  $\text{TiO}_2$  tetragonal phase of  $\text{ZrO}_2$  are observed. However, ZTODH shows pure phase of the sample shows  $hkl$  planes as that of ZTOU. Whereas very few diffraction peaks corresponding to monoclinic ( $(-111)$  at  $2\theta = 27.44^\circ$ ) and cubic ( $(200)$  at  $2\theta = 34.06^\circ$  and  $(220)$  at  $2\theta = 52.73^\circ$ ) phase of  $\text{ZrO}_2$ , as well as rutile phase of the  $\text{TiO}_2$  ( $(110)$  at  $2\theta = 28.46^\circ$ ) and ( $211$ ) at  $2\theta = 54.48^\circ$ ) are observed.

Debye–Scherrer's equation and Williamson–Hall (W–H) plot method were employed to determine the crystallite size of ZTOU (Fig. 3b) and ZTODH NPs (Fig. 3d) and this detail procedure was explained in the previous work.<sup>54</sup> In both ZTOU and ZTODH, high intense diffraction plane ( $111$ ) was used in Scherrer's equation to calculate the crystallite size. The crystallite size (calculated from Scherrer's equation and W–H plot method), strain and other structural parameters such as dislocation density ( $\delta$ ) and stacking fault of ZTOU and ZTODH are determined from equations given in previous work<sup>55</sup> are tabulated in Table 1. There is a slight difference in crystallite size values obtained from these two methods. This may be due to due to the fact that, the strain variable was believed to be zero in Scherrer's formula and the observed broadening of the diffraction peak was attributed to grain size reduction.

### 3.2 Morphological analysis

**3.2.1 SEM analysis of ZTOU and ZTODH nanorods.** The morphology of the surface, formation and distribution of the nanoparticles (NPs), elemental composition of the synthesized NPs can be obtained by performing SEM and EDAX analysis. Fig. 4a–c shows the SEM images of ZTOU NPs at different magnification. The surface morphology clearly indicates the formation of sharp edged nanorods of different lengths along with the irregular shaped agglomerated NPs. The width of the nanorods is varying between  $38.39$ – $61.17$  nm. The inset of Fig. 4c shows the particle size distribution histogram determined from the SEM images. NPs with size  $20$ – $200$  nm are distributed on the surface morphology. Fig. 4d shows the energy dispersive X-ray spectroscopy analysis (EDAX) indicating the presence of Zr, Ti and O atoms and also the absence of other impurities. The atomic percentage and weight percentage of the elements present in synthesized ZTOU NPs are provided in the inset table of Fig. 4d.

Fig. 5a–c shows the SEM images of ZTODH NPs at different magnification. The surface morphology clearly indicates the

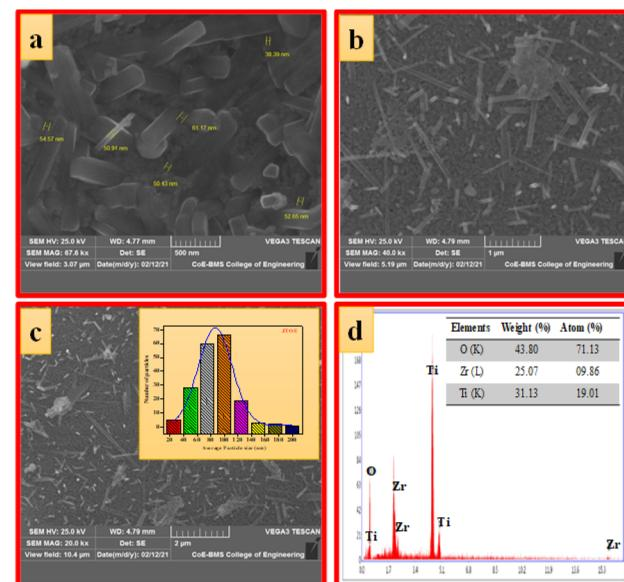


Fig. 4 (a–c) SEM images at different magnifications, (d) EDAX image (inset: elemental composition) of ZTOU nanorods.

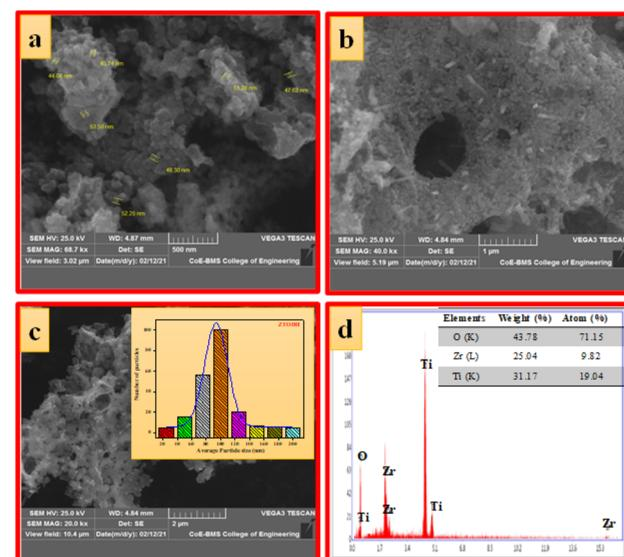


Fig. 5 (a–c) SEM images at different magnifications, (d) EDAX image (inset: elemental composition) of ZTODH nanorods.

presence of agglomerated and irregular shaped NPs with voids and pores which is the characteristic of combustion synthesis method. In addition to NPs, only few tiny nanorods are



observed. The size of the particle is varying between 44.08–52.25 nm. The histogram clearly shows that large number of NPs with 100 nm size are distributed on the surface (Fig. 5d). The EDAX spectra clearly confirms the presence of Zr, Ti and O elements indicating the absence of other impurities (Fig. 5d).

**3.2.2 TEM analysis of ZTOU and ZTODH nanorods.** Fig. 6a and 7a shows the TEM image of ZTOU and ZTODH. The TEM images of ZTOU clearly indicates the formation of both nanorods and NPs, whereas in ZTODH, nanorods are very thin. The HRTEM image of both ZTOU and ZTODH clearly shows the formation of well crystalline NPs (Fig. 6b and 7b). In Fig. 6c, the lattice fringes with the interplanar spacings 0.2912 nm, 0.1742 nm and 0.1792 nm corresponding to (111), (202) and (220) planes. In Fig. 7c, the lattice fringes with the interplanar spacings 0.2914 nm, 0.1738 nm, 0.1789 nm and 0.1418 nm corresponding to (111), (202), (220) and (023) planes. All these planes are reflected in the PXRD pattern. The average crystallite size of ZTOU and ZTODH was about 6 and 8 nm respectively, which is in good agreement with the size estimated by Scherrer's equation from the XRD pattern. PXRD and SAED pattern clearly confirms that both ZTOU and ZTODH are highly crystalline in nature (Fig. 6d and 7d). Even though in PXRD, few less intense peaks related to other phases of  $ZrO_2$  and  $TiO_2$  are observed, from HRTEM and SAED pattern, there was no

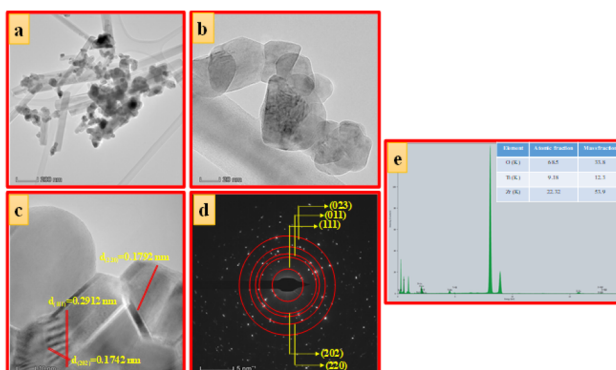


Fig. 6 (a) TEM images, (b and c) HRTEM images, (d) SAED pattern and (e) EDAX image of ZTOU nanorods.

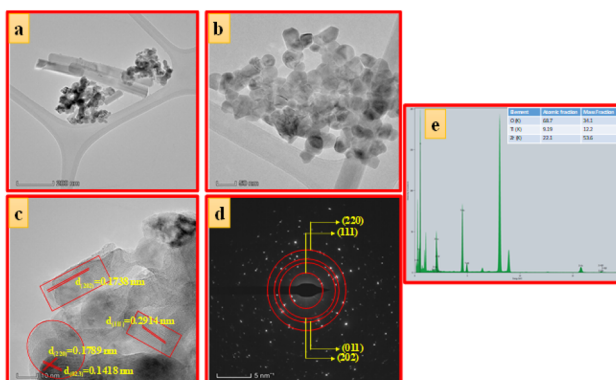


Fig. 7 (a) TEM images, (b and c) HRTEM images, (d) SAED pattern and (e) EDAX image of ZTODH nanorods.

evidence for the presence of other impurity phase such as peaks corresponding to monoclinic/cubic phases of  $ZrO_2$  or Anatase/Rutile/Brakite phase of  $TiO_2$ . The purity of the sample in turn observed in EDS spectrum which shows the presence of Zr, O and Ti elements. The atomic and weight percentage of these elements are provided in the inset table (Fig. 6e and 7e).

### 3.3 FTIR spectroscopic analysis of ZTOU and ZTODH

FTIR is a technique based on the measurement of the absorption of electromagnetic radiation with wavelengths within the mid-infrared region ( $4000$ – $400$   $cm^{-1}$ ).

When a molecule absorbs infrared radiation, the dipole moment changes and the molecule becomes IR active. The location of bands related to the strength and structure of bonds, as well as unique functional groups, can be found in a reported spectrum. Fig. 8 shows the FTIR spectra of ZTOU and ZTODH. The spectrum of ZTOU and ZTODH are almost similar but few bands are absent in ZTOU compared to ZTODH. The observed FTIR absorption peaks of ZTOU and ZTODH and their corresponding remarks with reference are provided in the Table 2. The studied optical parameters for ZTOU and ZTODH from the FTIR spectra is as shown in Fig. 9. Fig. 9a shows variation of measured extinction coefficient with the wavelength. From this variation it is observed that, extinction coefficient is smaller for the wavelength around 500 nm. Furthermore, there is small peak and then extinction coefficient increases with increase in wavelength. The variation of absorption coefficient ( $\alpha$ ) with the energy is as shown in Fig. 9b. The larger value of absorption is

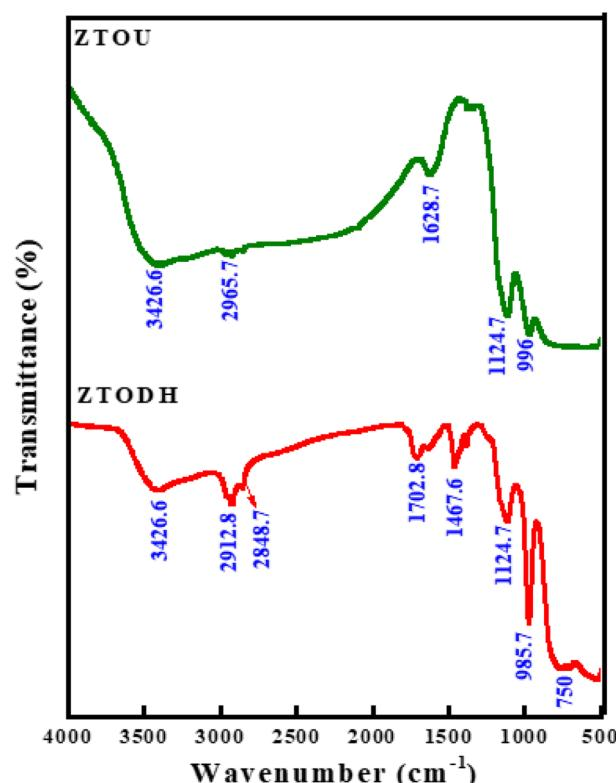
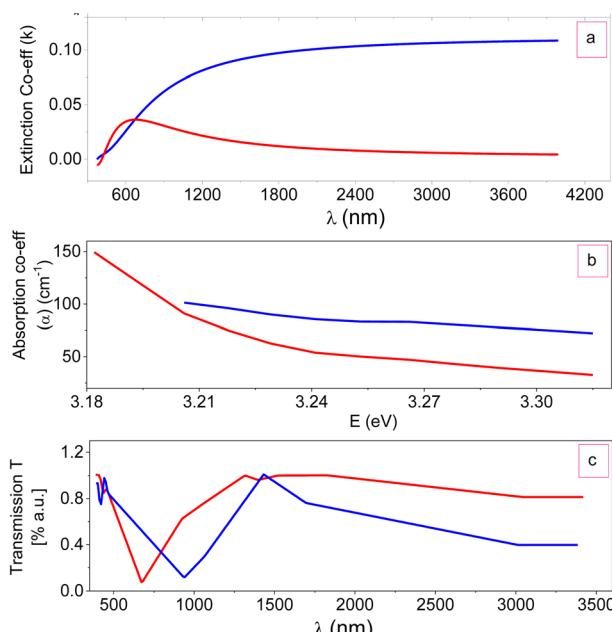


Fig. 8 FTIR spectra of ZTOU and ZTODH nanorods.

Table 2 Wavenumber of absorption peaks, remarks and references of ZTOU and ZTODH respectively

Absorption peaks wavenumber ( $\text{cm}^{-1}$ )		Remarks	Reference
ZTOU	ZTODH		
—	750	Ti–O characteristic bond	56
996	985.7	Ti–O characteristic bond	56
1124.7	1124.7	C=O bond	57
—	1467.6	O–H bending vibration	58
1628.7	1702.8	Stretching modes of saturated hydrocarbons	59
2965.7	2848.7	—	59
—	2912.8	—OH stretching vibration	60
3426.6	3426.6	—	60

Fig. 9 Optical parameters: (a) extinction coefficient ( $k$ ), (b) absorption coefficient ( $\alpha$ ) with energy and (c) transmission coefficient ( $T$ ) with wavelength of ZTO NPs.

found to be decreases with increase in energy. The percentage of transmission as a function of wavelength is as shown in the Fig. 9c. The percentage of transmission decreases with the increase in wavelength. Maximum value of transmission is found to 14.95% at 400 nm.

#### 3.4 UV-visible spectroscopic analysis and energy band gap calculation of ZTOU and ZTODH

UV-visible spectroscopic method is another relatively facile and low-cost characterization method that is often used for the study of nanoscale materials. It measures the intensity of light reflected/absorbed from a sample and compares it to the intensity of light reflected/absorbed from a reference material. The optical properties of the NMs are sensitive to size, shape, concentration, agglomeration state and refractive index near the nanoparticle surface, which makes UV-vis spectroscopy an important tool to identify, characterize and investigate these materials.

Fig. 10 depicts UV-visible spectra of ZTOU and ZTODH nanorods. The absorption spectra of ZTOU and ZTODH nanorod consists sharp intense absorption peak at 317 and 313 nm respectively, meanwhile no other less intense peaks are observed. The observed absorption peak in the UV region was observed due to electron transfer from the valence band to the conduction band. Tail formation in both the cases may be associated with the formation of new electronic levels between the valence band and conduction band promoted by the disordered structure of  $\text{ZrTiO}_4$  oxides.<sup>7</sup>

Using the absorption spectra, direct band gap was calculated by Wood and Tauc's relation.<sup>61</sup>

$$\alpha = \frac{A}{h\nu} (h\nu - E_g)^{\frac{1}{2}} \quad (3)$$

where  $\alpha$ ; absorption co-efficient,  $h\nu$ ; the photon energy,  $E_g$ ; the energy gap and  $A$ ; the constant depending on the type of transition. From the eqn (3)  $\alpha h\nu = 0$ ,  $E_g = h\nu$ . The energy gap is determined by plotting  $(\alpha h\nu)^2$  versus  $h\nu$  and finding the intercept on the  $h\nu$  axis by extrapolating the plot to  $(\alpha h\nu)^2 = 0$ . Inset of Fig. 10 shows the Wood and Tauc plot from which the direct band gap is obtained and was found to be 2.7 and 3.2 eV for ZTOU and ZTODH respectively. Both the valence and conduction

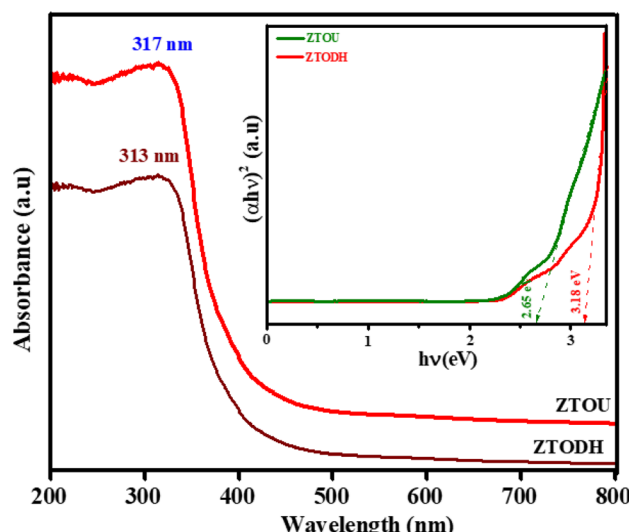


Fig. 10 UV-visible absorption spectra (inset: Wood and Tauc plot) of ZTOU and ZTODH nanorods.



bands of  $\text{TiO}_2$  have energy levels that are well inside the band gap of  $\text{ZrO}_2$ . When electrons are stimulated, the majority of electrons from the  $\text{ZrO}_2$  conduction band can easily migrate to the  $\text{TiO}_2$  conduction band, lowering the band gap.<sup>62,63</sup>

### 3.5 Photoluminescence studies of ZTOU and ZTODH

Inset of Fig. 11 shows the PLE excitation spectra of ZTOU and ZTODH nanorods. The excitation spectra of ZTOU consists peaks at 371, 398 and 403 nm. The PLE excitation spectra of ZTODH are observed at the same wavelength irrespective of the intensity. The emission spectra of ZTOU and ZTODH was recorded at an excitation wavelength of 350 nm (Fig. 11).

The PL emission spectra of ZTOU nanorods consists emission peaks at 361, 377, 405, 433, 459, 483, 528 and 541 nm. These peaks might have originated due to radiative recombination between defective levels situated within the band gap.<sup>11</sup> From the literature, it is observed that, PL spectra is the indication of disordered structure, once the system becomes ordered, PL signal disappears.<sup>7,64,65</sup> Moura *et al.*,<sup>4</sup> studied the intense PL emission spectra of calcium copper titanate samples. The order-disorder degree governed by  $[\text{TiO}_5]$  and  $[\text{TiO}_6]$  clusters plays an important role in the PL behavior at ambient temperature. Souza *et al.*,<sup>66</sup> observed the high intense green emission supported by symmetry break caused due to phase transformation in barium calcium titanate NPs. The structural disorder can favor PL emission with an excitation energy smaller than the crystalline gap energy.<sup>67</sup> However, this single effect is insufficient to improve intense visible PL at room temperature. The presence of localised states and the charge gradient (polarisation) create excellent conditions for trapping electrons and holes, allowing PL radiative recombination in the physically order-disordered ZTO nanorods.

The occurrence of PL emission peaks in the visible region is due to the presence of surficial and interfacial defects levels below the conduction band. As we know, the energy levels of  $\text{TiO}_2$  and  $\text{ZrTiO}_4$  lies well within the energy band gap of  $\text{ZrO}_2$ , electrons

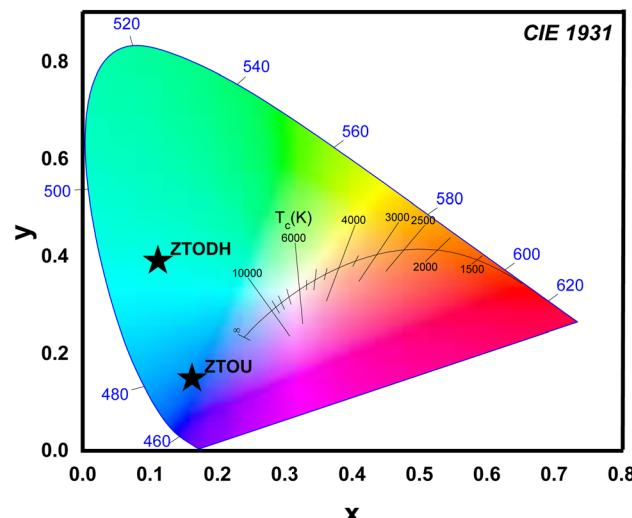


Fig. 12 CIE and CCT diagram of ZTOU and ZTODH nanorods.

reach the energy levels of surfacial  $\text{TiO}_2$  atoms, lying well below the energy levels of  $\text{ZrO}_2$ . This creates forbiddens for de-excitation in the surfacial titanium's and thereby increases the life time of the excitons which in turn favors the second excitation. During this second excitation, electrons reaches energy levels of  $\text{ZrO}_2$  and then get deexcites to ground level, with the emission of photon of energy greater than the excitation energy as shown in Fig. 12. The PL emission peak centred at 528 nm confirms the presence of sixfold oxygen-coordinated Ti ion ( $\text{TiO}_6$ ) with octahedral geometry in both ZTOU and ZTODH nanorods.<sup>65</sup> Eventhough, few other  $\text{TiO}_2$  and  $\text{ZrO}_2$  phases exists, PL intensity of ZTODH is less intense which inturn indicates the less recombination of electrons and holes or less defects.

One of the most important factors in determining the efficiency of synthesised nanophosphors is chromaticity coordinates. The emission color of ZTOU and ZTODH NMs were investigated by using 1931 CIE (Commission Internationale de L'Eclairage) system. The CIE coordinates are found to be (0.1612, 0.1546) and (0.111, 0.3902) for ZTOU and ZTODH located in the blue region and aqua green (Fig. 12). To identify the technical applicability, correlated color temperature (CCT) is determined from the CIE coordinates. The CCT describes the colour appearance of light emitted by a light source by comparing it to the colour of light emitted by a reference source when heated to a certain temperature. Lamps with a CCT rating of less than 3200 K are typically referred to as "hot," while those with a CCT of more than 4000 K are typically referred to as "cold". In the present study, the calculated CCT value of ZTOU and ZTODH were found to be 4181 and 17 697 K. This clearly indicates that the present ZTOU and ZTODH can be used as a blue and aqua green phosphor material which might be a potential candidate for display/LED application.

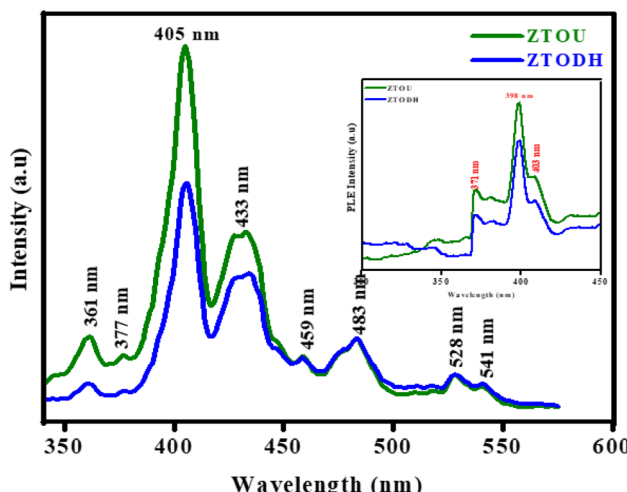


Fig. 11 PL emission spectra ( $\lambda_{\text{ex}} = 350$  nm) (inset: excitation spectra) of ZTOU and ZTODH nanorods.

### 3.6 Analysis of measured X-ray/gamma absorption properties of ZTOU and ZTODH

X-ray/gamma absorption is quantified by the mass attenuation coefficient ( $\mu/\rho$ ). The measured mass attenuation coefficient for



Table 3 Comparison of measured mass attenuation coefficient with that of theory for ZTOU and ZTODH

Source	Energy (MeV)	Mass attenuation coefficient ( $\text{cm}^2 \text{g}^{-1}$ )			
		ZTOU		ZTODH	
Theo.	Exp.	Theo.	Exp.		
<sup>56</sup> Ba	0.081	0.9039	$1.523 \pm 0.07615$	0.9623	$1.743 \pm 0.08715$
	0.276	0.1279	$0.424 \pm 0.0212$	0.2425	$0.527 \pm 0.02635$
	0.356	0.1063	$0.182 \pm 0.0091$	0.1327	$0.194 \pm 0.0097$
<sup>22</sup> Na	0.511	0.085	$0.084 \pm 0.0042$	0.084	$0.082 \pm 0.0041$
<sup>137</sup> Cs	0.6615	0.0757	$0.076 \pm 0.0038$	0.0761	$0.078 \pm 0.0039$
<sup>60</sup> Co	1.173	0.05599	$0.056 \pm 0.0028$	0.05682	$0.059 \pm 0.00295$
	1.332	0.0526	$0.053 \pm 0.00265$	0.054	$0.057 \pm 0.00285$

ZTOU and ZTODH are compared with standard Hubbel data<sup>68-70</sup> and it is shown in Table 3. From observed that measured mass attenuation coefficient for ZTOU and ZTODH comparable with standard data. It is clearly observed from the Table 3 that above 356 keV X-ray/gamma ray interaction energy, the measured mass attenuation coefficient agrees well with the theoretical value whereas slight deviation is observed below 356 keV. The measured mass attenuation coefficient was used to compute the X-ray/gamma shielding parameters such as linear attenuation coefficient ( $\mu$ ), mean free path  $\lambda$ , half-value layer (HVL), tenth value layer (TVL), effective atomic number ( $Z_{\text{eff}}$ ), effective electron number ( $N_e$ ), energy absorption buildup factor (EABF), kinetic energy released in matter (KERMA), specific gamma ray constant (SGR), specific absorption factor (SAF) and

radiation protection efficiency (RPE) with that of the theoretical values in the energy range 0.081–1.332 MeV. Fig. 13 shows the comparison of measured shielding properties with that of the theory.

The variation demonstrates the  $\mu/\rho$ ,  $\mu$  value's quick decline with increasing photon energy (Fig. 13a and b). The photoelectric process, which predominates at lower energies, is mostly responsible for the quick fall in MAC and linear attenuation coefficient at lower energies. Similar variation is also observed with effective atomic number, electron density and EABF (Fig. 13f, g and h). The thickness of a shield tenth value layers (TVL) and half value layer (HVL) was found to increases with increase in energy of the X-ray/Gamma radiation (Fig. 13d and e). The mean free path increases slowly with increase in the energy of photon (Fig. 13c). The similar variation is also observed for KERMA and SGR (Fig. 13i and j). SAF and RPE was studied at different thickness and for different photon energy (Fig. 13k and l). As the thickness increases, SAF value was found to be high whereas with increase in photon energy, initially at lower energy, it increases slowly and thereafter remains constant. There is a risk that secondary radiation will be produced as the gamma photon moves through the medium, raising SAF's value. As the thickness increases, incident gamma/X-ray loses its energy and hence decrease in relative dose is observed. At 1 mm thickness, as the photon energy increases, the RPE value goes on decreases and the same variations are observed with increase in the thickness of the absorbing material.

Theoretical values are based on the Hubbel data<sup>68-70</sup> which was used to explain interaction of X-ray/gamma with atoms of size ( $10^{-6}$  m). In the present experiment, we have taken the target with atomic size ( $10^{-9}$  m). The measured shielding parameters agrees well with the theory above 356 keV X-ray/gamma-ray interaction. This is may be due to the fact that atom/particle size will not affect the interaction of X-ray/gamma-ray on the ZTO NPs above 356 keV. Whereas, measured shielding parameters shows deviation with theory below 356 keV. This may be due to the fact that the atom/particle size plays an important role below 356 keV. It can be concluded that the atom/particle size affect the interaction of X-ray/gamma ray with the target medium. Furthermore an

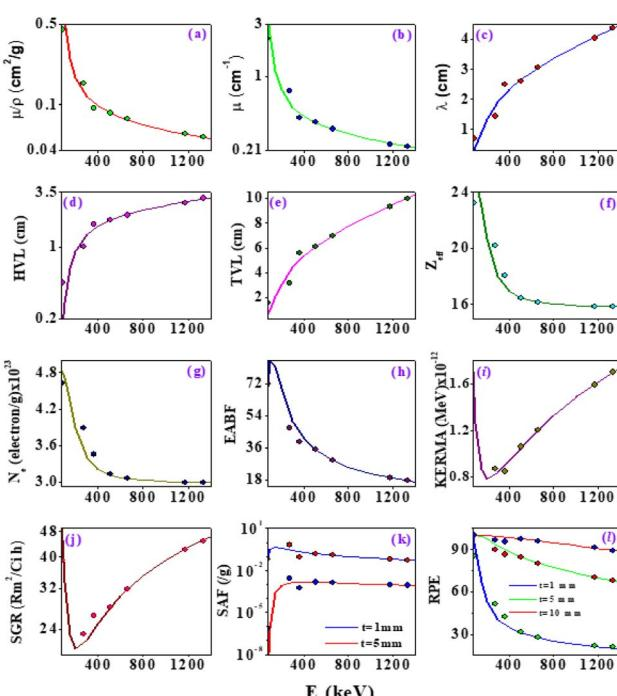


Fig. 13 Comparison of measured shielding properties such as (a)  $\mu/\rho$ , (b)  $\mu$ , (c)  $\lambda$ , (d) HVL, (e) TVL, (f)  $Z_{\text{eff}}$ , (g)  $N_e$ , (h) EABF, (i) KERMA, (j) SGR, (k) SAF and (l) RPE with that of the theoretical values in the energy range 0.081–1.332 MeV.



accurate theory is necessary to explain the X-ray/gamma ray interaction with the nanomaterials.

### 3.7 Antibacterial properties

The NPs were inspected against both Gram-positive (*Bacillus cereus*) and the Gram-negative (*Pseudomonasaeruginosa*) bacteria for antibacterial studies. The minimum inhibition concentration (MIC) was calculated by the formula given in the materials and methods. Viability test was conducted on two food borne pathogens: *Bacillus cereus* and *Pseudomonasaeruginosa*, Fig. 14a and b shows the variation of number of colonies with quantity of ZTOU and ZTODH NPs in *Bacillus cereus* and *Pseudomonasaeruginosa* respectively. Jose *et al.*,<sup>14</sup> investigated the antibacterial properties against *Escherichiacoli* and *Staphylococcusepidermidis* of titanate nanotubes modified with silver NPs. Sales *et al.*,<sup>12</sup> studied the antibacterial properties of silver-cerium titanate nanotubes on Gram positive and Gram negative bacteria. Fig. 14c and d shows the variation of percentage of inhibition with ZTOU and ZTODH NPs quantity in *Bacillus cereus* and *Pseudomonasaeruginosa* respectively which was carried out to determine MIC value. The results showed that as the concentration of the urea and ODH increases, the viability of the organisms decreases gradually in dose dependent manner. The minimum inhibitory concentration for the urea is 15 mg ml<sup>-1</sup> against *Bacillus cereus* and *Pseudomonasaeruginosa* is also at 15 mg ml<sup>-1</sup> concentrations where both the molecules inhibits >90% of the bacterial growth. The Fig. 14e and f shows the growth comparison of *Bacillus cereus* in control plate and the plate containing 10 mg urea and ODH respectively. ODH shows relatively less antimicrobial activity compared to that ZTODH. Investigation was further carried out to determine antibacterial activity by using agar well diffusion assay. A clear zone of inhibition was shown by the urea against *Bacillus cereus* which measures about 22 mm in size at 15 mg ml<sup>-1</sup> concentration. The material showed fairly good

antimicrobial activity compared to streptomycin. There are reports previously of similar NPs showing the antimicrobial activity of cobalt ferrites.<sup>71</sup> These molecules once assimilated will be metabolized in to catechol-like compounds, which could inhibit the growth of bacterial colonies.

### 3.8 Electrochemical analysis of ZTOU and ZTODH

#### 3.8.1 Electrochemical investigation of ZTOU and ZTODH.

The ZTOU and ZTODH nanorods were studied to explore its potential application in supercapacitor electrodes with effective sensor material by performing electrochemical measurements using three-electrode system in 0.1 M HCl electrolyte. Adimule *et al.*,<sup>72</sup> discussed the impedance and CV analysis of a gadolinium titanate. A cyclic voltammetry (CV) and electrochemical impedance spectroscopy (EIS) were applied in the electrochemical measurements. The CV studies provide information about load efficiency and reversibility of the electrode response.<sup>73</sup> In order to ensure the stability of the MFC<sub>3</sub> sample, CV experiments were performed at varied scan rates (10–50 mV s<sup>-1</sup>) utilising 0.1 M HCl electrolytes. The CV curves at different scan rate with potential ranges from -0.5 to 1.0 V for ZTOU and ZTODH are shown in Fig. 15a and c respectively. As the scan rate increases, the quasi rectangular shape also found to increase. After detail CV analysis, it is found that the synthesized ZTOU nanorods shows very good redox peaks than that of ZTODH. This observation shows that the synthesized ZTOU nanorods exhibits highly enhanced electro-catalytic efficiency and robust electron transfer with increase in anodic and cathodic peak currents.

The measured electrochemical impedance spectral (EIS) for ZTOU and ZTODH are shown in Fig. 15b and d respectively. The encircled area in the EIS curve is directly proportional to the capacitance and resistance. From these figures, it is observed that the encircled area in the EIS spectra is larger for ZTOU than that of ZTODH. Eventually, the capacitance and resistance of ZTOU is larger than that of ZTODH.

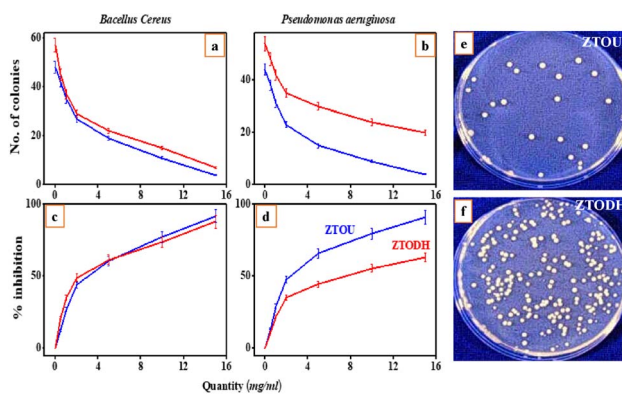


Fig. 14 Antibacterial properties of ZTOU nanorods. Variation of number of colonies with different concentration (mg mL<sup>-1</sup>) of ZTOU nano particles in (a) *Bacillus cereus* and (b) *Pseudomonasaeruginosa* bacteria. Variation of percentage of inhibition with different concentration (mg mL<sup>-1</sup>) of ZTODH NPs in (c) *Bacillus cereus* and (d) *Pseudomonasaeruginosa* bacteria. Zone of inhibition (e) by the ZTOU NPs and (f) by the ZTODH against *Bacillus cereus* which measures about 22 mm in size at 15 mg mL<sup>-1</sup> concentration.

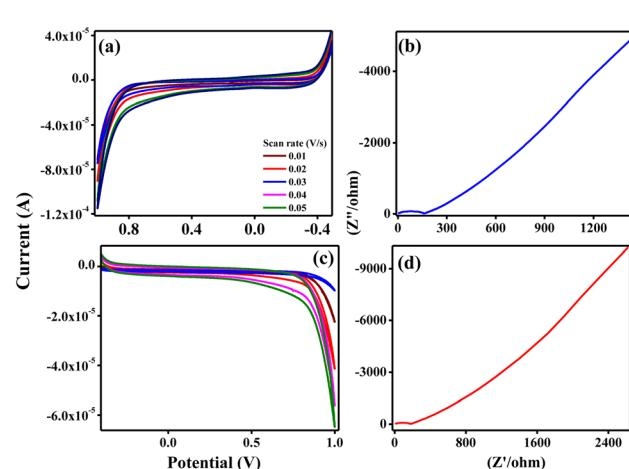


Fig. 15 Cyclic voltammetry and electrochemical impedance spectroscopy analysis (a) cyclic voltammetry response for the ZTOU (b) Nyquist plots obtained for ZTOU (c) cyclic voltammetry response for the ZTODH (d) Nyquist plots obtained for ZTODH.



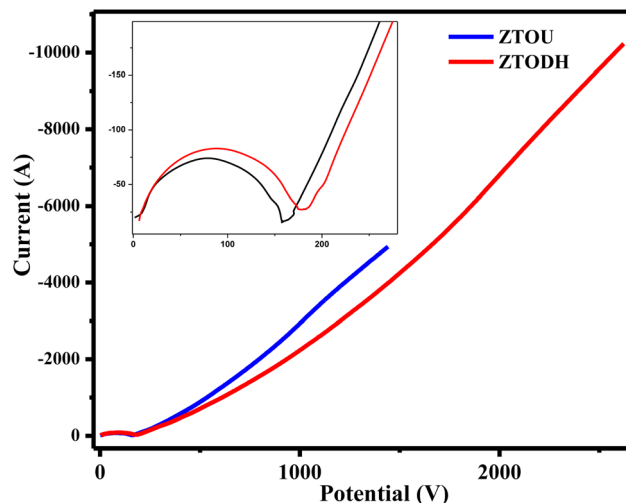


Fig. 16 EIS analysis of ZTOU and ZTODH nanorods.

EIS analysis shows the electrical conductivity of prepared ZTO nanorods and its Nyquist plots displays a semicircle in the higher frequency region along with a vertical line in the lower frequency region. However, the smaller semicircle in diameter and straight line towards Y-axis associates to the higher capacitance of ZTO nanorods. The radius of the arc is proportional to the resistance at the interface layer on the working electrode's external surface.<sup>74</sup> The separation of photo induced charges was more effective and charge transfer was higher across the electrode/electrolyte contact when the arc radius was small. The charge-transfer resistance for prepared nanorods ZTOU and ZTODH are found to be 151.6  $\Omega$ , and 184.5  $\Omega$  respectively. According to the hopping mechanism, changes in the mobility of charge carriers cause current to flow from one atom to the next in ZTO nanorods.<sup>75</sup> Therefore, the prepared ZTOU nano rods show smaller semicircle and a better vertical line when compared to that of ZTODH and it is clearly depicted in the Fig. 16.

### 3.9 Supercapacitor properties of ZTOU and ZTODH

The galvanostatic charge-discharge curves (GCD) in addition to CV tests was carried out to confirm the supercapacitor performance and discussed as follows: the GCD assistances in measuring the specific capacitance of the electrodes by the following equation:

$$C_{sp} = \frac{I \times \Delta t}{m \times \Delta V} \quad (4)$$

where  $C_{sp}$  = specific capacitance estimated from GCD curve (F g<sup>-1</sup>),  $I$  = response current density,  $\Delta t$  = discharge time,  $m$  = mass of the active materials on single electrode and  $\Delta V$  = potential range during the charge-discharge measurement. At a current density of 0.1 A g<sup>-1</sup>, the charge-discharge curves of the synthesised ZTOU and ZTODH nanorods with voltage windows ranging between 0.0–0.7 V are shown in Fig. 17a and b. For the sake of comparison, both the curves are shown in the Fig. 17c.

Teoh *et al.*,<sup>76</sup> analysed the the effectiveness of barium titanate

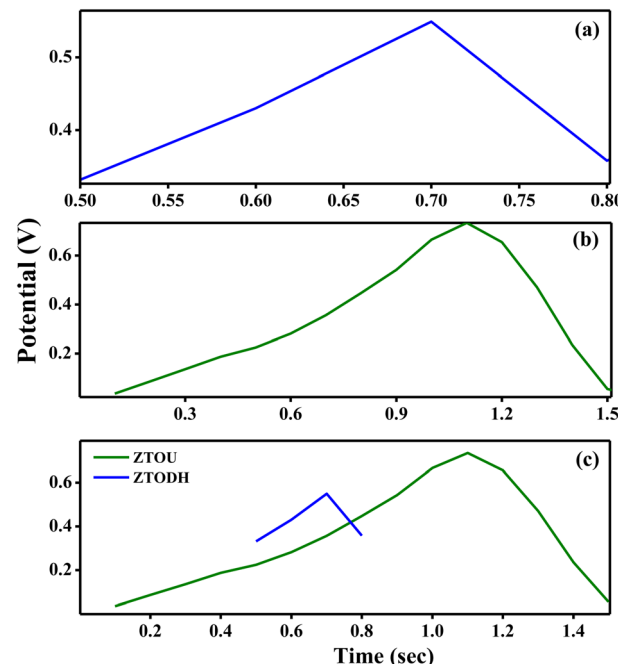


Fig. 17 Charging and discharging curves for (a) ZTOU nanorods (b) ZTODH nanorods (c) both ZTOU and ZTODH nanorods.

added to polymer electrolytes made of corn starch for use in double layer capacitors. Wu *et al.*,<sup>77</sup> analysed energy storage properties of sodium bismuth titanate for use in dielectric capacitor applications. From this CV pattern analysis, it is observed that ZTOU nanorods shows longest discharge duration compared to that of ZTODH nanorods. Hence we can conclude that ZTOU nanorods are suitable material for supercapacitor applications.

### 3.10 ZrTiO<sub>4</sub> as a chemical sensor

Further, the qualitative electrochemical measurements of ZTO nanorods were extended towards chemical sensor (paracetamol and ascorbic acid) detections. Jin *et al.*,<sup>78</sup> studied the gas sensing properties of iron and copper titanate NPs. Rashid *et al.*,<sup>79</sup> investigated the acetone sensing properties of zinc titanate NPs. Ferraz *et al.*,<sup>80</sup> studied the titanate nanowire based nanostructured screen-printed electrodes for biosensing applications. The electrochemical behaviour of paracetamol and ascorbic acid with increase in concentration from 1 to 7 mM was examined using graphite modified MFC<sub>3</sub> electrode at a scan rate of 30 mV s<sup>-1</sup>. For comparative purpose, the sensor material was tested under 0.1 M HCl as electrolytes.

CV response of ZTOU and ZTODH nanorods in paracetamol and ascorbic acid is shown in Fig. 18a and b and Fig. 18c and d at 0.1 M HCl electrolyte respectively. A slight anodic peak at -0.4 V was observed without any sensor. When paracetamol of 1 mM was added in 0.1 M HCl solution, there was an extreme change in the peak position of ZTOU with two oxidation peaks at -0.19 and 0.15 V along with two reduction peaks at 0.033 and 0.78 V (Fig. 18a). However, in ZTODH oxidation peaks are observed at -0.206 and 0.153 V along with two reduction peaks



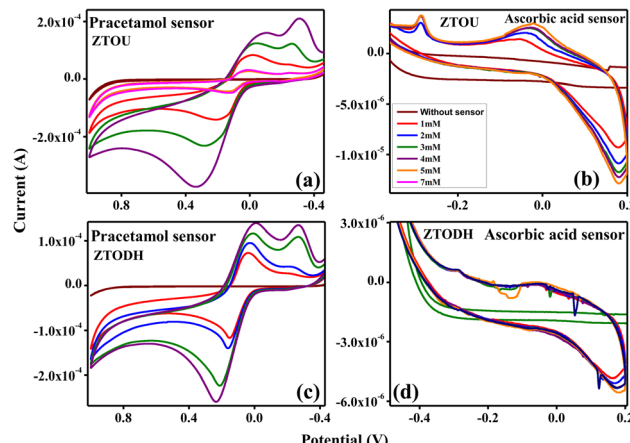


Fig. 18 Chemical sensor sensitivity of ZTO nanorods: cyclic voltammetry response of (a) ZTOU in paracetamol (b) ZTOU in ascorbic acid. (c) ZTODH in paracetamol, (d) ZTODH in ascorbic acid.

at  $-0.236$  and  $0.029$  V. As the concentration of paracetamol increases from  $1$  mM to  $7$  mM, the peak position also increases in both ZTOU and ZTODH. Hence, at a very low concentration of  $1$  mM, the graphite modified  $\text{MFC}_3$  electrode can be utilized to sense paracetamol. When the same experiment is repeated for ascorbic acid, as a sensor material, initially for ZTOU, at  $1$  mM concentration, there was a small oxidation peak at  $-0.079$  V along with a reduction peak at  $-0.28$  V (Fig. 18b) which was due to the electrode interface sense of ascorbic acid in the solution. As the concentration increases, the oxidation and reduction peaks almost remains in the same positions with slight increase in the intensity indicating the good sensing nature of ascorbic acid by the electrode. From these figures, it is observed that there are more significant changes in redox peaks of prepared ZTOU nanorods for paracetamol and ascorbic acid than that of ZTODH nanorods. Eventually, we can conclude that ZTOU nanorods shows good chemical sensing activity. This study is first of its kind that reports the good chemical sensing activity of ZTOU using three-electrode system in  $0.1$  M HCl electrolyte.

## 4. Summary

The  $\text{ZrTiO}_4$  nanorods are synthesized by solution combustion method using urea and ODH as a fuel and calcined at  $700$  °C. The synthesized samples are characterized by different techniques. The PXRD pattern confirms the orthorhombic structure along with the presence of few monoclinic, cubic phases of  $\text{ZrO}_2$  and rutile phase of the  $\text{TiO}_2$  are observed. The crystallite size was calculated by using both Debye Scherrer's equation method ( $6$  and  $8$  nm) and W-H plot method ( $8$  and  $10$  nm). The surface morphology of ZTOU and ZTODH consists of nanorods along with NPs. The estimated crystallite size from the TEM, HRTEM matches well with that of PXRD. The direct energy band gap was calculated using Wood and Tauc's relation was found to be  $2.7$  and  $3.2$  eV for ZTOU and ZTODH respectively. The photoluminescence emission peaks ( $\lambda = 350$  nm), CIE and CCT of ZTOU and ZTODH clearly confirms that the present

nanophosphor might be a good nanophosphor material for cool blue light emitting diodes. Furthermore, ZTOU showed good antimicrobial activity compared to streptomycin which was used treat a number of bacterial infections. The detailed X-ray/gamma ray absorption parameters are established. The electrochemical investigation of synthesised ZTOU and ZTODH nanorods were carried out to confirms its supercapacitor nature and electrochemical sensor sensitivity. Compared to ZTODH, ZTOU with graphite paste electrode shows a good supercapacitor nature as well as electrochemical sensor sensitivity towards the action for paracetamol and ascorbic acid detections. This excellent performance of ZTO NPs might be due to the presence of both nonorods as well as NPs.

## Conflicts of interest

There is no conflicts to declare.

## References

- 1 W. D. Kingery, H. K. Bowen, and D. R. Uhlmann, *Introduction to ceramics*, John Wiley & Sons, 1976, vol. 17.
- 2 A. Xu, H. Liu, G. Yi, N. Feng and H. Li, Clustering-enhanced, nonconventional photoluminescence from a silicone surfactant, *Chem. Commun.*, 2023, **59**, 3558.
- 3 D.-A. Chang, P. Lin and T.-Y. Tseng, Optical properties of  $\text{zrtio}_4$  films grown by radio-frequency magnetron sputtering, *J. Appl. Phys.*, 1995, **77**, 4445.
- 4 F. Moura, A. Simoes, R. Deus, M. Silva, J. A. Varela and E. Longo, Intense photoluminescence emission at room temperature in calcium copper titanate powders, *Ceram. Int.*, 2013, **39**, 3499.
- 5 L. De Haart, A. De Vries and G. Blasse, On the photoluminescence of semiconducting titanates applied in photoelectrochemical cells, *J. Solid State Chem.*, 1985, **59**, 291.
- 6 E. R. Leite, E. C. Paris, F. Pontes, C. A. Paskocimas, E. Longo, F. Sensato, C. D. Pinheiro, J. A. Varela, P. S. Pizani, C. Campos, *et al.*, The origin of photoluminescence in amorphous lead titanate, *J. Mater. Sci.*, 2003, **38**, 1175.
- 7 P. R. de Lucena, E. R. Leite, F. M. Pontes, E. Longo, P. S. Pizani and J. A. Varela, Photoluminescence: A probe for short, medium and long-range self-organization order in  $\text{zrtio}_4$  oxide, *J. Solid State Chem.*, 2006, **179**, 3997.
- 8 L. M. Oanh, D. B. Do, N. M. Hung, D. V. Thang, D. T. Phuong, D. T. Ha and N. Van Minh, Formation of crystal structure of zirconium titanate  $\text{zrtio}_4$  powders prepared by sol-gel method, *J. Electron. Mater.*, 2016, **45**, 2553.
- 9 B. Lokesh and N. M. Rao, Effect of Cu-doping on structural, optical and photoluminescence properties of zinc titanates synthesized by solid state reaction, *J. Mater. Sci.: Mater. Electron.*, 2016, **27**, 4253.
- 10 M.-S. Zhang, J. Yu, J. Chu, Q. Chen and W. Chen, Microstructures and photoluminescence of barium titanate nanocrystals synthesized by the hydrothermal process, *J. Mater. Process. Technol.*, 2003, **137**, 78.



11 A. Sangeetha, B. Nagabhushana, *et al.*, Comparative study of photoluminescence of single and mixed phase zrtio4 prepared by solution combustion and polymeric precursor method, *J. Mol. Struct.*, 2019, **1179**, 126.

12 D. A. Sales, T. M. Marques, A. Ghosh, S. B. Gusmão, T. L. Vasconcelos, C. Luz-Lima, O. P. Ferreira, L. M. Hollanda, I. S. Lima, E. C. Silva-Filho, *et al.*, Synthesis of silver-cerium titanate nanotubes and their surface properties and antibacterial applications, *Mater. Sci. Eng. C*, 2020, **115**, 111051.

13 T. Eiampongpaiboon, W. O. Chung, J. D. Bryers, K.-H. Chung and D. C. Chan, Antibacterial activity of gold-titanates on gram-positive cariogenic bacteria, *Acta Biomater. Odontol. Scand.*, 2015, **1**, 51.

14 M. Jose, P. Sienkiewicz, K. Szymańska, D. Darowna, D. Moszyński, Z. Lendzion-Bieluń, K. Szymański and S. Mozia, Influence of preparation procedure on physicochemical and antibacterial properties of titanate nanotubes modified with silver, *Nanomaterials*, 2019, **9**, 795.

15 Z. Xu, M. Li, X. Li, X. Liu, F. Ma, S. Wu, K. Yeung, Y. Han and P. K. Chu, Antibacterial activity of silver doped titanate nanowires on ti implants, *ACS Appl. Mater. Interfaces*, 2016, **8**, 16584.

16 D. Hobbs, M. Barnes, R. Pulmano, K. Marshall, T. Edwards, M. Bronikowski and S. Fink, Strontium and actinide separations from high level nuclear waste solutions using monosodium titanate 1. simulant testing, *Sep. Sci. Technol.*, 2005, **40**, 3093.

17 M. Nyman and D. T. Hobbs, A family of peroxy-titanate materials tailored for optimal strontium and actinide sorption, *Chem. Mater.*, 2006, **18**, 6425.

18 R. R. Davis, D. T. Hobbs, R. Khashaba, P. Sehkar, F. N. Seta, R. L. Messer, J. B. Lewis and J. C. Wataha, Titanate particles as agents to deliver gold compounds to fibroblasts and monocytes, *J. Biomed. Mater. Res., Part A*, 2010, **93**, 864.

19 J. C. Wataha, D. T. Hobbs, P. E. Lockwood, R. R. Davis, M. C. Elvington, J. B. Lewis and R. L. Messer, Peroxititanates for biodelivery of metals, *J. Biomed. Mater. Res., Part B*, 2009, **91**, 489.

20 A. B. Stoian, M. Vardaki, D. Ionita, M. Enachescu, M. Prodana, O. Brancoveanu and I. Demetrescu, Nanopores and nanotubes ceramic oxides elaborated on titanium alloy with zirconium by changing anodization potentials, *Ceram. Int.*, 2018, **44**, 7026.

21 N. Saulacic, D. Bosshardt, M. Bornstein, S. Berner and D. Buser, Bone apposition to a titanium-zirconium alloy implant, as compared to two other titanium-containing implants, *Eur. Cells Mater.*, 2012, **23**, 273.

22 M. Vardaki, S. Mohajernia, A. Pantazi, I. C. Nica, M. Enachescu, A. Mazare, I. Demetrescu and P. Schmuki, Post treatments effect on tizr nanostructures fabricated via anodizing, *J. Mater. Res. Technol.*, 2019, **8**, 5802.

23 S. Mohseni, M. Aghayan, A. Ghorani-Azam, M. Behdani and A. Asoodeh, Evaluation of antibacterial properties of barium zirconate titanate (bzt) nanoparticle, *Braz. J. Microbiol.*, 2014, **45**, 1393.

24 R. R. Bhosale, D. K. Gaikwad, P. P. Pawar and M. N. Rode, Interaction studies and gamma-ray properties of some low-z materials, *Nucl. Technol. Radiat. Prot.*, 2016, **31**, 135.

25 M. Ambika, N. Nagaiah and S. Suman, Role of bismuth oxide as a reinforcer on gamma shielding ability of unsaturated polyester based polymer composites, *J. Appl. Polym. Sci.*, 2017, **134**, 44657.

26 L. Yu, P. L. Yap, A. Santos, D. Tran and D. Losic, Lightweight bismuth titanate (bi4ti3o12) nanoparticle-epoxy composite for advanced lead-free x-ray radiation shielding, *ACS Appl. Nano Mater.*, 2021, **4**, 7471.

27 M. N. Amin, I. Ahmad, A. Abbas, K. Khan, M. G. Qadir, M. Iqbal, A. M. Abu-Arab and A. A. Alabdullah, Estimating radiation shielding of fired clay bricks using ann and gep approaches, *Materials*, 2022, **15**, 5908.

28 P. Saini, M. Arora, G. Gupta, B. K. Gupta, V. N. Singh and V. Choudhary, High permittivity polyaniline-barium titanate nanocomposites with excellent electromagnetic interference shielding response, *Nanoscale*, 2013, **5**, 4330.

29 I. Akkurt and H. O. Tekin, Radiological parameters of bismuth oxide glasses using the phy-x/psd software, *Emerging Mater. Res.*, 2020, **9**, 1020.

30 Y. S. Rammah, A. Kumar, K. A.-A. Mahmoud, R. El-Mallawany, F. I. El-Agawany, G. Susoy and H. O. Tekin, Sno-reinforced silicate glasses and utilization in gamma-radiation-shielding applications, *Emerging Mater. Res.*, 2020, **9**, 1000.

31 D. Sariyer and R. Küçer, Effect of different materials to concrete as neutron shielding application, *Acta Phys. Pol.*, A, 2020, **137**, 477.

32 Y. Y. Çelen and A. Evcin, Synthesis and characterizations of magnetite-borogypsum for radiation shielding, *Emerging Mater. Res.*, 2020, **9**, 770.

33 E. Bakker and M. Telting-Diaz, Electrochemical sensors, *Anal. Chem.*, 2002, **74**, 2781.

34 O. Zahhaf, G. D'Ambrogio, A. Giunta, M.-Q. Le, G. Rival, P.-J. Cottinet and J.-F. Capsal, Molten-state dielectrophoretic alignment of eva/batio3 thermoplastic composites: Enhancement of piezo-smart sensor for medical application, *Int. J. Mol. Sci.*, 2022, **23**, 15745.

35 X. Kang, J. Wang, H. Wu, J. Liu, I. A. Aksay and Y. Lin, A graphene-based electrochemical sensor for sensitive detection of paracetamol, *Talanta*, 2010, **81**, 754.

36 M. Knochen, J. Giglio and B. F. Reis, Flow-injection spectrophotometric determination of paracetamol in tablets and oral solutions, *J. Pharm. Biomed. Anal.*, 2003, **33**, 191.

37 P. S. Selvan, R. Gopinath, V. Saravanan, N. Gopal, A. S. Kumar and K. Periyasamy, Simultaneous estimation of paracetamol and aceclofenac in combined dosage forms by rp-hplc method, *Asian J. Chem.*, 2007, **19**, 1004.

38 D. Easwaramoorthy, Y.-C. Yu and H.-J. Huang, Chemiluminescence detection of paracetamol by a luminol-permanganate based reaction, *Anal. Chim. Acta*, 2001, **439**, 95.



39 W. Wei, X. Cui, W. Chen and D. G. Ivey, Manganese oxide-based materials as electrochemical supercapacitor electrodes, *Chem. Soc. Rev.*, 2011, **40**, 1697.

40 M. P. Down, S. J. Rowley-Neale, G. C. Smith and C. E. Banks, Fabrication of graphene oxide supercapacitor devices, *ACS Appl. Energy Mater.*, 2018, **1**, 707.

41 C. Ng, H. Lim, Y. Lim, W. Chee and N. Huang, Fabrication of flexible polypyrrole/graphene oxide/manganese oxide supercapacitor, *Int. J. Energy Res.*, 2015, **39**, 344.

42 A. K. Tomar, G. Singh and R. K. Sharma, Charge storage characteristics of mesoporous strontium titanate perovskite aqueous as well as flexible solid-state supercapacitor cell, *J. Power Sources*, 2019, **426**, 223.

43 S. Moghiminia, H. Farsi and H. Raissi, Comparative optical and electrochemical studies of nanostructured  $\text{NiTiO}_3$  and  $\text{NiTiO}_3\text{-TiO}_2$  prepared by a low temperature modified sol-gel route, *Electrochim. Acta*, 2014, **132**, 512.

44 G. A. Kallawar, D. P. Barai and B. A. Bhanvase, Bismuth titanate based photocatalysts for degradation of persistent organic compounds in wastewater: A comprehensive review on synthesis methods, performance as photocatalyst and challenges, *J. Cleaner Prod.*, 2021, **318**, 128563.

45 X. Sun and Y. Li, Synthesis and characterization of ion-exchangeable titanate nanotubes, *Chem. - Eur. J.*, 2003, **9**, 2229.

46 L. Torrente-Murciano, A. A. Lapkin and D. Chadwick, Synthesis of high aspect ratio titanate nanotubes, *J. Mater. Chem.*, 2010, **20**, 6484.

47 J. Zhang, Y.-a. Wang, J. Yang, J. Chen and Z. Zhang, Microwave-assisted synthesis of potassium titanate nanowires, *Mater. Lett.*, 2006, **60**, 3015.

48 C. Liu, B. Zou, A. J. Rondinone and Z. J. Zhang, Sol-gel synthesis of free-standing ferroelectric lead zirconate titanate nanoparticles, *J. Am. Chem. Soc.*, 2001, **123**, 4344.

49 J.-Y. Lin, C.-C. Hsu, H.-P. Ho and S.-h. Wu, Sol-gel synthesis of aluminum doped lithium titanate anode material for lithium ion batteries, *Electrochim. Acta*, 2013, **87**, 126.

50 E. Carlos, R. Martins, E. Fortunato and R. Branquinho, Solution combustion synthesis: towards a sustainable approach for metal oxides, *Chem. - Eur. J.*, 2020, **26**, 9099.

51 R. Abbas, K. D. Martinson, T. Y. Kiseleva, G. P. Markov, P. Y. Tyapkin and V. I. Popkov, Effect of fuel type on the solution combustion synthesis, structure, and magnetic properties of  $\text{YIG}$  nanocrystals, *Mater. Today Commun.*, 2022, **32**, 103866.

52 B. C. Reddy, H. Manjunatha, Y. Vidya, K. Sridhar, U. M. Pasha, L. Seenappa, C. Mahendrakumar, B. Sadashivamurthy, N. Dhananjaya, B. Sankarshan, *et al.*, Synthesis and characterization of multi functional nickel ferrite nano-particles for x-ray/gamma radiation shielding, display and antimicrobial applications, *J. Phys. Chem. Solids*, 2021, **159**, 110260.

53 G. Jayaprakasha, T. Selvi and K. Sakariah, Antibacterial and antioxidant activities of grape (*Vitis vinifera*) seed extracts, *Food Res. Int.*, 2003, **36**, 117.

54 Y. Vidya, K. Anantharaju, H. Nagabhushana, S. Sharma, H. Nagaswarupa, S. Prashantha, C. Shivakumara, *et al.*, Combustion synthesized tetragonal  $\text{ZrO}_2$ :  $\text{Eu}^{3+}$  nanophosphors: structural and photoluminescence studies, *Spectrochim. Acta, Part A*, 2015, **135**, 241.

55 K. Gurushantha, K. Anantharaju, S. Sharma, H. Nagaswarupa, S. Prashantha, K. V. Mahesh, L. Renuka, Y. Vidya and H. Nagabhushana, Bio-mediated sm doped nano cubic zirconia: Photoluminescent, judd-ofelt analysis, electrochemical impedance spectroscopy and photocatalytic performance, *J. Alloys Compd.*, 2016, **685**, 761.

56 R. Ashiri, Detailed ft-ir spectroscopy characterization and thermal analysis of synthesis of barium titanate nanoscale particles through a newly developed process, *Vib. Spectrosc.*, 2013, **66**, 24.

57 N. Akhtar, H. M. Rafique, S. Atiq, S. Aslam, A. Razaq and M. Saleem, Dielectric based energy storage capacity of sol-gel synthesized  $\text{SrTiO}_4$  nanocrystallites, *Ceram. Int.*, 2018, **44**, 6705.

58 H. Z. Akbas, Z. Aydin, I. H. Karahan, T. Dilsizoglu, and S. Turgut, Process control using ft-ir analysis of  $\text{BaTiO}_3$  from ultrasonically activated  $\text{BaCO}_3$  and  $\text{TiO}_2$ , in *Proceedings of 17th Research World International Conference*, Riyadh, Saudi Arabia, 19th June 2016, 2016.

59 R. B. Bohn, S. A. Sandford, L. J. Allamandola and D. P. Cruikshank, Infrared spectroscopy of triton and pluto ice analogs: The case for saturated hydrocarbons, *Icarus*, 1994, **111**, 151.

60 E. F. Sulaikah, R. Kurniawan, M. F. Pradipta, W. Trisunaryanti and A. Syoufian, Cobalt doping on zirconium titanate as a potential photocatalyst with visible-light-response, *Indones. J. Chem.*, 2020, **20**, 911.

61 L. Ley, Photoemission and optical properties, *The Physics of Hydrogenated Amorphous Silicon II*, 1984, vol. 61.

62 L. J. Tomar and B. Chakrabarty, Synthesis, structural and optical properties of  $\text{TiO}_2\text{-ZrO}_2$  nanocomposite by hydrothermal method, *Adv. Mater. Lett.*, 2013, **4**, 64.

63 B. Neppolian, Q. Wang, H. Yamashita and H. Choi, Synthesis and characterization of  $\text{ZrO}_2\text{-TiO}_2$  binary oxide semiconductor nanoparticles: application and interparticle electron transfer process, *Appl. Catal., A*, 2007, **333**, 264.

64 I. Souza, A. Simoes, E. Longo, J. A. Varela and P. Pizani, Photoluminescence at room temperature in disordered  $\text{Ba}_{0.50}\text{Sr}_{0.50}\text{TiO}_{3}$  thin films, *Appl. Phys. Lett.*, 2006, **88**, 211911.

65 G. Freitas, L. Soledade, E. Leite, E. Longo, P. Pizani, T. Boschi, C. Paskocimas, J. A. Varela, D. Melo, M. Cerqueira, *et al.*, Photoluminescence in amorphous zirconium titanate, *Appl. Phys. A*, 2004, **78**, 355.

66 A. Souza, R. Silva, G. Santos, M. Moreira, D. Volanti, S. Teixeira and E. Longo, Photoluminescence of barium-calcium titanates obtained by the microwave-assisted hydrothermal method (mah), *Chem. Phys. Lett.*, 2010, **488**, 54.

67 M. Anicete-Santos, M. S. Silva, E. Orhan, M. S. Góes, M. A. Zaghe, C. O. Paiva-Santos, P. S. Pizani, M. Cilense, J. A. Varela and E. Longo, Contribution of structural order-



disorder to the room-temperature photoluminescence of lead zirconate titanate powders, *J. Lumin.*, 2007, **127**, 689.

68 J. H. Hubbell and S. M. Seltzer, *Tables of x-ray mass attenuation coefficients and mass energy-absorption coefficients 1 kev to 20 mev for elements z= 1 to 92 and 48 additional substances of dosimetric interest*, 1995.

69 M. Berger, *Xcom: photon cross sections database*, 2010, <http://www.nist.gov/pml/data/xcom/index.cfm>.

70 L. Gerward, N. Guilbert, K. B. Jensen and H. Levring, X-ray absorption in matter. reengineering xcom, *Radiat. Phys. Chem.*, 2001, **60**, 23.

71 M. M. Naik, H. B. Naik, G. Nagaraju, M. Vinuth, K. Vinu and R. Viswanath, Green synthesis of zinc doped cobalt ferrite nanoparticles: Structural, optical, photocatalytic and antibacterial studies, *Nano-Struct. Nano-Objects*, 2019, **19**, 100322.

72 V. M Adimule, D. Bhowmik and A. Haramballi Jagadeesha, Synthesis, impedance and current-voltage spectroscopic characterization of novel gadolinium titanate nano structures, *Adv. Mater. Lett.*, 2021, **12**, 1.

73 B. Shruthi, B. Madhu, V. B. Raju, S. Vynatheya, B. V. Devi, G. Jayashree and C. Ravikumar, Synthesis, spectroscopic analysis and electrochemical performance of modified  $\beta$ -nickel hydroxide electrode with cuo, *J. Sci.: Adv. Mater. Devices*, 2017, **2**, 93.

74 S. Meena, K. Anantharaju, Y. Vidya, L. Renuka, B. Uma, S. Sharma, S. S. More, *et al.*, Enhanced sunlight driven photocatalytic activity and electrochemical sensing properties of ce-doped mnfe<sub>2</sub>o<sub>4</sub> nano magnetic ferrites, *Ceram. Int.*, 2021, **47**, 14760.

75 M. A. Rehman, I. Yusoff and Y. Alias, Fluoride adsorption by doped and un-doped magnetic ferrites cucefe<sub>2</sub>-x<sub>0</sub>4: Preparation, characterization, optimization and modeling for effectual remediation technologies, *J. Hazard. Mater.*, 2015, **299**, 316.

76 K. Teoh, C.-S. Lim, C. W. Liew and S. Ramesh, Preparation and performance analysis of barium titanate incorporated in corn starch-based polymer electrolytes for electric double layer capacitor application, *J. Appl. Polym. Sci.*, 2016, **133**, 43275.

77 Y. Wu, Y. Fan, N. Liu, P. Peng, M. Zhou, S. Yan, F. Cao, X. Dong and G. Wang, Enhanced energy storage properties in sodium bismuth titanate-based ceramics for dielectric capacitor applications, *J. Mater. Chem. C*, 2019, **7**, 6222.

78 J. Jin, Y. Zhang, G. Li, Z. Chu and G. Li, Synthesis and enhanced gas sensing properties of iron titanate and copper titanate nanomaterials, *Mater. Chem. Phys.*, 2020, **249**, 123016.

79 S. S. A. Abdul Haroon Rashid, Y. M. Sabri, A. E. Kandjani, C. J. Harrison, R. K. Canjeevaram Balasubramanyam, E. Della Gaspera, M. R. Field, S. K. Bhargava, A. Tricoli, W. Włodarski, *et al.*, Zinc titanate nanoarrays with superior optoelectrochemical properties for chemical sensing, *ACS Appl. Mater. Interfaces*, 2019, **11**, 29255.

80 H. C. Ferraz, D. F. Machado and N. S. de Resende, Nanostructured screen-printed electrodes based on titanate nanowires for biosensing applications, *Mater. Sci. Eng. C*, 2017, **70**, 15.

